



1

2

3

## Lipid Removal in Deuterium Metabolic Imaging (DMI)

4

using Spatial Prior Knowledge.

5

6 Robin A. de Graaf <sup>1,2</sup>, Yanning Liu <sup>2</sup>, Zachary A. Corbin <sup>3</sup>, Henk M. De Feyter <sup>1</sup>

7

8 Departments of Radiology and Biomedical Imaging <sup>1</sup>, Biomedical Engineering <sup>2</sup> and Neurology <sup>3</sup>

9

Magnetic Resonance Research Center

10

Yale University School of Medicine

11

New Haven, Connecticut, USA

12

13

14 Address correspondence to:

15 Robin A. de Graaf, Ph.D.

16 Magnetic Resonance Research Center

17 Department of Radiology and Biomedical Imaging

18 Yale University School of Medicine

19 300 Cedar Street, P.O. Box 208043

20 New Haven, CT 06520-8043, USA

21 Tel: (203) 785-6203

22 Fax: (203) 785-6643

23 E-mail: [robin.degraaf@yale.edu](mailto:robin.degraaf@yale.edu)

24

25

26

27 Word count: 4,866 (abstract, main body, figure legends)

28 Short title: Robust Processing of Deuterium Metabolic Imaging



1 **ABSTRACT**

2 Deuterium Metabolic Imaging (DMI) is a novel method to generate spatial maps depicting dynamic metabolism  
3 of deuterated substrates, such as [6,6'-<sup>2</sup>H<sub>2</sub>]-glucose, and their metabolic products, like <sup>2</sup>H-lactate. While DMI  
4 acquisition methods are simple and robust, DMI processing still requires expert user interaction, for example in  
5 the removal of extracranial natural abundance <sup>2</sup>H lipid signals that interfere with metabolism-linked <sup>2</sup>H-lactate  
6 formation. Here we pursue the use of MRI-based spatial prior knowledge on brain and non-brain/skull locations  
7 to provide robust and objective lipid removal. Magnetic field heterogeneity was accounted for using DMI-derived  
8 surrogate B<sub>0</sub> and B<sub>1</sub> maps, as well as through subdivision of the skull region into smaller compartments.  
9 Adequate lipid removal with an average suppression of 90.5 ± 11.4 % is achieved on human brain *in vivo* without  
10 perturbation of the metabolic profile in brain voxels, thereby allowing the generation of distinct and reliable  
11 metabolic maps on patients with brain tumors.

12 Key words: Deuterium, Deuterium Metabolic Imaging (DMI), natural abundance lipids, human brain, spatial  
13 prior knowledge

14

15

16

17

18

19

20

21

22

23

24

25

26

27

28

29



## 1 1. INTRODUCTION

2 Deuterium Metabolic Imaging (DMI) is a recent method to map the spatial distribution of  $^2\text{H}$ -enriched substrates  
3 and their metabolic products in health and disease (De Feyter et al., 2018; Kaggie et al., 2022; Adamson et al.,  
4 2023). The most commonly used substrate,  $[6,6\text{-}^2\text{H}_2]$ -glucose, has shown promise to offer unique metabolic  
5 insights in brain tumors (De Feyter et al., 2018; Adamson et al., 2023), stroke (Straathof et al., 2021), brown  
6 adipose tissue (Riis-Vestergaard et al., 2020), heart (Wang et al., 2021), preeclampsia (Markovic et al., 2021)  
7 and a range of tumors outside the brain (Kreis et al., 2020; Veltien et al., 2021). Other  $^2\text{H}$ -enriched substrates,  
8 such as  $^2\text{H}_9$ -choline and  $[2,3\text{-}^2\text{H}_2]$ -fumarate, can provide insights into tumor proliferation (Veltien et al., 2021; Ip  
9 et al., 2023) and cell death (Hesse et al., 2021), respectively. DMI sets itself apart from other metabolic imaging  
10 modalities such as  $^1\text{H}$ ,  $^{13}\text{C}$ , hyperpolarized  $^{13}\text{C}$  and  $^{31}\text{P}$  MRSI, through its simple and robust acquisition methods.  
11 The low natural abundance of deuterium eliminates the need for water and lipid suppression, whereas the  
12 sparsity of  $^2\text{H}$  MR spectra reduces the magnetic field homogeneity requirements, thereby enabling the acquisition  
13 of 3D DMI across the entire human head with high-quality spectra at all locations (De Feyter et al., 2018; Ruhm  
14 et al., 2021; Liu et al., 2022; Seres Roig et al., 2022).

15 Processing of DMI is generally straightforward, with high-quality quantification achieved using least-squares  
16 curve fitting with a limited number of Lorentzian lines (De Feyter et al., 2018). DMI of  $[6,6\text{-}^2\text{H}_2]$ -glucose  
17 metabolism generally requires four signals for  $^2\text{H}$ -labeled water, glucose (Glc), the combined signal from  
18 glutamate and glutamine (Glx) and lactate (Lac). A metabolic map of Lac or a ratio map of Lac/(Lac + Glx)  
19 provides high-contrast images of pathological metabolism as described for brain and other tumors (De Feyter et  
20 al., 2018), as well as stroke (Straathof et al., 2021). With sufficient sensitivity, as seen near radiofrequency (RF)  
21 coil receive elements, natural abundance  $^2\text{H}$  lipid signals originating from the skull will produce a detectable MR  
22 signal. While these small lipid signals do not cause the widespread contamination throughout the brain as seen  
23 for  $^1\text{H}$  MRSI (Tkáč et al., 2021), they can lead to artifactual intensity in Lac and Lac-Glx ratio maps as the Lac  
24 and lipids signals share near-identical chemical shifts. Lipid suppression in human brain MRSI studies can be  
25 achieved through pulse sequence modifications (inner volume selection, outer volume suppression, longer echo-  
26 times), additional hardware (higher-order gradient coils, crusher coils) or post-processing methods. While pulse  
27 sequence modifications and hardware solutions can give excellent lipid suppression (Tkáč et al., 2021), the  
28 requirements for DMI are generally modest, making post-processing methods a logical choice while still retaining  
29 the simple DMI acquisition method. Many post-processing methods utilize MRI-based prior knowledge on the  
30 lipid spatial location to achieve lipid removal and include dual density reconstruction (Hu et al., 1994; Metzger et  
31 al., 1999), data extrapolation (Haupt et al., 1996), L2 regularization (Bilgic et al., 2014) and Spectroscopic  
32 Localization by Imaging (SLIM, (Hu et al., 1988)) and its variants (Liang and Lauterbur, 1991; Von Kienlin and  
33 Mejia, 1991; Bashir and Yablonskiy, 2006; Khalidov et al., 2007; Zhang et al., 2012; Passeri et al., 2014; Adany  
34 et al., 2016, 2021).



1 Here we propose to use the SLIM algorithm (Hu et al., 1988) because it can (1) be applied to standard, 3D  
2 phase-encoded DMI without data acquisition modifications, (2) remove extracranial lipids without perturbing the  
3 brain metabolic profile and (3) be extended to provide regional brain signals from anatomy-matched  
4 compartments. The processing pipeline, including MRI brain/skull segmentation, generation of DMI-based  
5 surrogate  $B_0$  and  $B_1$  maps and SLIM-based regional signal removal, can be fully automated and provides a  
6 robust and objective tool to accelerate the inclusion of DMI in a clinical MR workflow.

7

## 8 **2. METHODS**

### 9 **2.1. Workflow and algorithm**

10 SLIM belongs to a class of post-processing methods that constrains the MRSI reconstruction with spatial prior  
11 knowledge derived from anatomical MRIs. The MRSI acquisition is formulated as a linear model whereby the  
12 acquired k-space data  $P$  is the linear sum of ROI-specific signals  $C$  weighted by a gradient and position-  
13 dependent factor  $G$  according to

14

$$15 \quad P = G.C \quad [1]$$

16  $P$  is the measured  $N_{\text{enc}} \times N_{\text{time}}$  k-space data matrix, with  $N_{\text{enc}}$  representing the total number of phase-encoding  
17 gradient combinations (i.e., number of k-space encodings) and  $N_{\text{time}}$  representing the number of complex,  
18 spectroscopic time domain points.  $C$  is an  $N_{\text{ROI}} \times N_{\text{time}}$  matrix containing the time-domain signals from each of  
19 the  $N_{\text{ROI}}$  compartments, the sum of which comprises the entire object under investigation (e.g., human head,  
20 including brain and skull areas). The shape of the ROIs can be arbitrary with  $N_{\text{ROI}} \leq N_{\text{enc}}$ .  $G$  is a  $N_{\text{enc}} \times N_{\text{ROI}}$   
21 encoding matrix describing the amount of signal dephasing across a given compartment  $k$ , during phase-  
22 encoding step  $m$  according to

23

$$24 \quad G_{k,m} = \sum_{r \in \text{ROI}_k} e^{2\pi i k_m r} \quad \text{with } k = 1 \dots N_{\text{ROI}}, m = 1 \dots N_{\text{enc}} \quad [2]$$

25

26  $k_m$  represents the time integral of phase-encoding gradient  $m$ . The SLIM algorithm calculates the ROI-specific  
27 signal  $C$  from the measured data  $P$  according to

28

$$29 \quad C = G^{-1}.P \quad [3]$$

30



1 whereby the inverse of  $G$  can be obtained through singular value decomposition (SVD). If the object under  
2 investigation can be decomposed into  $C_{ROI}$  *homogeneous* compartments, without any requirements on  
3 homogeneity *between* compartments, then the SLIM algorithm produces  $C_{ROI}$  signals from the ROIs without any  
4 contamination from other compartments.

5 Fig. 1 summarizes how the outlined algorithm can be utilized to achieve lipid removal in DMI. Based on  
6 anatomical MRIs (Fig. 1A), the human head can be segmented into  $N_{brain}$  ROIs and  $N_{skull}$  ROIs (Fig. 1B/C), after  
7 which the gradient encoding matrix  $G$  can be calculated for each ROI. With the measured DMI data (Fig. 1D) as  
8 input  $P$ , the ROI-specific signals  $C$  can be calculated via Eq. [3] (Fig. 1G). The  $N_{skull}$  signals can be used to  
9 reconstruct, via Eq. [1], a skull MRSI dataset (Fig. 1H), which can be subtracted from the original MRSI to provide  
10 a skull-free, lipid-suppressed MRSI dataset (Fig. 1I).

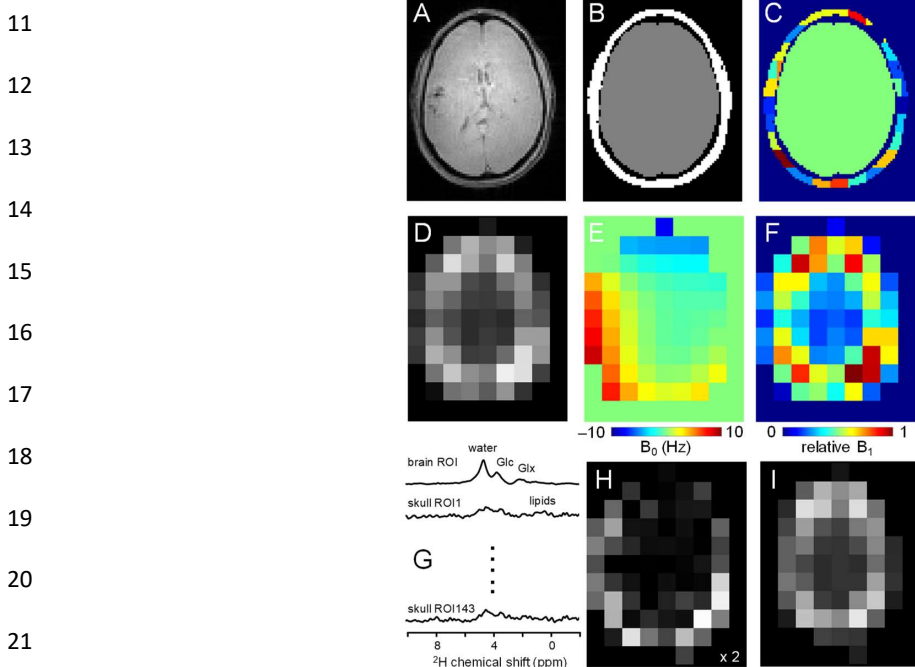


**Figure 1 – Lipid removal workflow.** (A) Anatomical MRI and (B) brain and non-brain/skull ROIs. (C) To accommodate heterogeneity in the skull ROI, it is sub-divided into 125-175 ROIs of 3.5 – 8.5 mL. (D)  $^2\text{H}$ -water map obtained through numerical integration of each pixel in a  $9 \times 13 \times 11$  DMI dataset. (E)  $^2\text{H}$ -water line shift map and (F) relative  $^2\text{H}$ -water intensity map. (G) Compartment-specific signals from one brain ROI and 143 skull ROIs are the primary output of the SLIM algorithm. (H) DMI reconstructed from the 143 skull ROI signals, which can be subtracted from (D) the original DMI to yield (I) a skull (and lipid) free DMI dataset.

22  
23 When all ROIs are homogeneous, the suppression of skull-based signals is expected to be perfect.  
24 Unfortunately, the requirement for homogeneous compartments is rarely encountered experimentally due to  
25 variations in metabolic composition and  $B_0$  and  $B_1$  magnetic fields across the sample. This heterogeneity is a  
26 violation of the linear model (Eq. [1]) and will lead to contamination (or ‘bleeding’) between ROIs (Liang and



1 Lauterbur, 1993; Von Kienlin and Mejia, 1991) and thus an incomplete removal of skull-based lipids. Several  
2 strategies have been developed to address the issue of signal heterogeneity. Multiple methods incorporate prior  
3 knowledge on magnetic field heterogeneity from  $B_0$  and/or  $B_1$  map into the SLIM processing pipeline (Bashir and  
4 Yablonskiy, 2006; Khalidov et al., 2007; Passeri et al., 2014; Adany et al., 2016). Other methods seek to optimize  
5 the k-space encoding scheme to minimize bleeding between ROIs (Von Kienlin and Mejia, 1991; Zhang et al.,  
6 2012), whereas another strategy rests on subdividing larger ROIs to decrease the heterogeneity across any one  
7 ROI (Adany et al., 2021; Dong and Hwang, 2006).

8 Here we employ two strategies, namely (1) the subdivision of the non-brain ROI into smaller, more homogeneous  
9 compartments and (2) the incorporation of prior knowledge on known  $B_0$  and  $B_1$  magnetic field heterogeneity.  
10 Following the segmentation of brain and non-brain ROIs, the latter is sub-divided further (Fig. 1C) by multiplying  
11 the ROI with an equidistant 3D grid. A minimum ROI volume is enforced by combining adjacent ROIs for which  
12 at least one falls below a minimum threshold. The effect of the ROI size and number of ROIs on the localization  
13 performance can be quantitatively evaluated through calculation of the spatial response function (SRF, (Von  
14 Kienlin and Mejia, 1991)) according to

15

$$16 \quad SRF_k(r) = \sum_{m=1}^{N_{enc}} G_{k,m}^{-1} e^{2\pi i k_m r} \quad \text{with } k = 1 \dots N_{ROI} \quad [4]$$

17

18 The SRF is a complex function that depicts the spatial extent of each ROI given a set of k-space encodings,  
19 whereby the net SRF contribution of a given ROI is zero across all other ROIs.

20 The incorporation of  $B_0$  and  $B_1$  magnetic field heterogeneity is achieved through a modification of the encoding  
21 matrix (Eq. [2]) according to

22

$$23 \quad G_{k,m,n} = \sum_{r \in ROI_k} B_1(r) e^{2\pi i k_m r} \cdot e^{2\pi i B_0(r) t_n} \quad \text{with } n = 1 \dots N_{time} \quad [5]$$

24

25 Note that  $G$  essentially converts from a time-independent  $N_{enc} \times N_{ROI}$  matrix to a time-dependent  $N_{enc} \times N_{ROI} \times$   
26  $N_{time}$  matrix, providing unique encoding for each (spectroscopic) time point  $n$ . In Eq. [5]  $B_0(r)$  represents a spatial  
27  $B_0$  magnetic field maps (in Hz) and  $B_1(r)$  represents a relative signal intensity (0 ... 1) with contributions from the  
28 transmit  $B_1^+$  and receive  $B_1^-$  magnetic fields. While high-resolution  $B_0$  and  $B_1$  maps can be obtained with routine  
29 MR methods for  $^1H$  MRSI, the low-sensitivity DMI data prevents a comparable implementation. The calculation  
30 of surrogate  $B_0$  and  $B_1$  maps (Figs. 1E and F) from the measured DMI data will be described next.

31



## 1 **2.2. Simulations**

2 To evaluate the effectiveness of extracranial lipid suppression and intracranial metabolite retention, simulations  
3 were performed on brain and non-brain ROIs segmented from  $T_2$ -weighted MRIs of five human subjects. To limit  
4 the overall calculation times, all simulations were performed on a single 2D slice. The brain ROIs were manually  
5 segmented into gray matter (GM), white matter (WM) and cerebrospinal fluid (CSF). A pathological ROI (e.g.,  
6 tumor, stroke) with a random size (72 – 148 % of a nominal MRSI voxel), shape and position was placed inside  
7 the brain ROI. With ten random pathology ROI variations per subject, a total of fifty datasets were created for  
8 simulation.

9 Heterogeneity in the  $B_0$  and  $B_1$  magnetic fields can significantly affect the reconstruction performance and  
10 simulations were extended with typical distributions found across the human head *in vivo*. As  $^2\text{H}$ -based  $B_0$  and  
11  $B_1$  maps are not readily available, DMI-derived  $B_0$  and  $B_1$  maps were determined on five subjects by measuring  
12 the  $^2\text{H}$  water line shift and  $^2\text{H}$  water intensity in each pixel across a 2D slice, respectively. The maps were  
13 parameterized with a fourth order 2D polynomial fit to set the  $B_0$  and  $B_1$  distribution average and range. Each of  
14 the 50 simulated datasets was constructed with unique  $B_0$  and  $B_1$  distributions, calculated from randomly selected  
15 polynomial coefficients characterizing the *in vivo* ranges. To further accommodate  $B_0$  and  $B_1$  heterogeneity, the  
16 skull ROI was divided into multiple smaller ROIs. The division was initiated by multiplying the skull ROI by a grid  
17 of uniform voxels (e.g., 20 x 20 mm). The resulting skull ROIs were combined with the nearest neighbor ROI  
18 when the ROI volume was below a minimum threshold volume (e.g., 40% of a nominal volume). By adjusting  
19 the grid size, the number of skull ROIs was varied from 1 to 50 to determine the optimal setting.

20 Using knowledge on the spatial ROIs,  $B_0$  and  $B_1$  distribution and MRSI k-space encoding, DMI datasets were  
21 calculated as a 9 x 13 spatial matrix and 512 complex points acquired over a 1.0 kHz spectral width using a  
22 single, well-resolved resonance line per compartment in addition to a water signal present in all compartments.  
23 Optional Gaussian noise could be added to the entire 9 x 13 x 512 time domain DMI dataset. SLIM processing  
24 (i.e., Eq. [3]) resulted in ROI-specific signals  $C$ , from which the non-brain ROI signals were selected to calculate  
25 a non-brain DMI dataset. Subtraction of the non-brain DMI dataset from the experimentally measured DMI  
26 produced a lipid-free, brain-only DMI dataset. All data analysis is based on numerical integration of the well-  
27 separated spectral MR signals representing water, lipids and metabolites.

28

## 29 **2.3. Human studies *in vivo***

30 All human studies were approved by the Yale University Institutional Review Board. All scans were performed  
31 on a 4 T Magnex magnet (Magnex Scientific Ltd.) interfaced to a Bruker Avance III HD spectrometer running on  
32 ParaVision 6 (Bruker Instruments). The system was equipped with 67-cm-diameter Magnex gradients capable  
33 of switching 30 mT/m in 1.1 ms. RF transmission and reception were conducted with a 28.5-cm-diameter  
34 transverse electromagnetic (TEM) volume coil tuned to the proton frequency (170.5 MHz) for MRI and shimming.



1 Deuterium RF reception at 26.2 MHz was achieved with a four-coil phased array that was driven as a single RF  
2 coil during RF transmission. The four  $8 \times 10$  cm rectangular  $^2\text{H}$  array elements were positioned equidistantly on  
3 an  $18 \times 25$  cm elliptical former that was positioned within the  $^1\text{H}$  TEM coil.

4 DMI was acquired with a pulse-acquire method, extended with 3D phase-encoding according to a spherical k-  
5 space sampling pattern. A total of 491 phase encoding steps were acquired to generate a  $9 \times 13 \times 11$  DMI  
6 dataset in circa 27 min with 8 mL nominal resolution (TR = 333 ms, 10 averages). All DMI scans were preceded  
7 by anatomical MRIs and second-order SH shimming over the entire brain. Natural abundance DMI data was  
8 acquired on three subjects without the administration of deuterated substrates. On two subjects, including one  
9 patient with an intracranial glioblastoma tumor,  $[6,6\text{-}^2\text{H}_2]$ -glucose dissolved in water was administered orally  
10 (0.75 g/kg) after which the metabolic profile was sampled with DMI 90 – 120 min later. Brain and non-brain (i.e.,  
11 skull) ROIs were semi-automatically segmented from 3D gradient-echo MRIs (TR/TE = 25/6 ms).

12 Processing of the *in vivo* DMI datasets is similar to that described for simulated data with a few noticeable  
13 differences. Firstly, whereas all *in vivo* DMI data is acquired as a  $9 \times 13 \times 11$  matrix over a field-of-view of  $180 \times$   
14  $260 \times 220$  mm (XYZ), the limited length (80 mm) of the  $^2\text{H}$  RF elements only provided  $^2\text{H}$  signal in 3 to 4 planes  
15 in the Z direction. As a result, ROIs were only generated for spatial positions where the  $^2\text{H}$  water intensity was  
16 at least 5% of the maximum intensity in the entire 3D dataset. Secondly, the brain ROI was not divided into  
17 tissue-specific compartments (e.g., GM, WM, CSF) as simulations (see Results) demonstrated that this step did  
18 not affect lipid suppression and metabolite retention. Thirdly, the skull ROI was divided according to a 3D grid of  
19 nominal DMI voxels without further optimization. ROIs below a minimum volume threshold (40% of nominal)  
20 were merged with nearest neighbor ROIs, resulting in 128-177 skull ROIs across all subjects. Fourthly, signal  
21 quantification is based on non-linear least-squares fitting using a linear combination model of Lorentzian-shaped  
22 signals for  $^2\text{H}$ -labeled water, glucose, glutamate+glutamine (Glx) and lactate.  $^2\text{H}$  MR spectra are fitted with a  
23 (fixed) linear phase roll due to the delayed  $^2\text{H}$  acquisition caused by the phase-encoding gradient. While the  
24 overall linewidths are unconstrained to accommodate magnetic field heterogeneity, the linewidth of metabolites  
25 are linked (within a  $[-2 \dots +5]$  Hz range) to the water linewidth. All spectral fitting was performed in DMIWizard,  
26 a graphical user interface programmed in Matlab (The MathWorks, Natick, MA, USA) and freely available to the  
27 MR community. Finally, in the evaluation of metabolite retention, only pure-brain pixels are considered. For lipid  
28 suppression, partial skull pixels are also considered even though can lead to an underestimation of the real  
29 suppression.

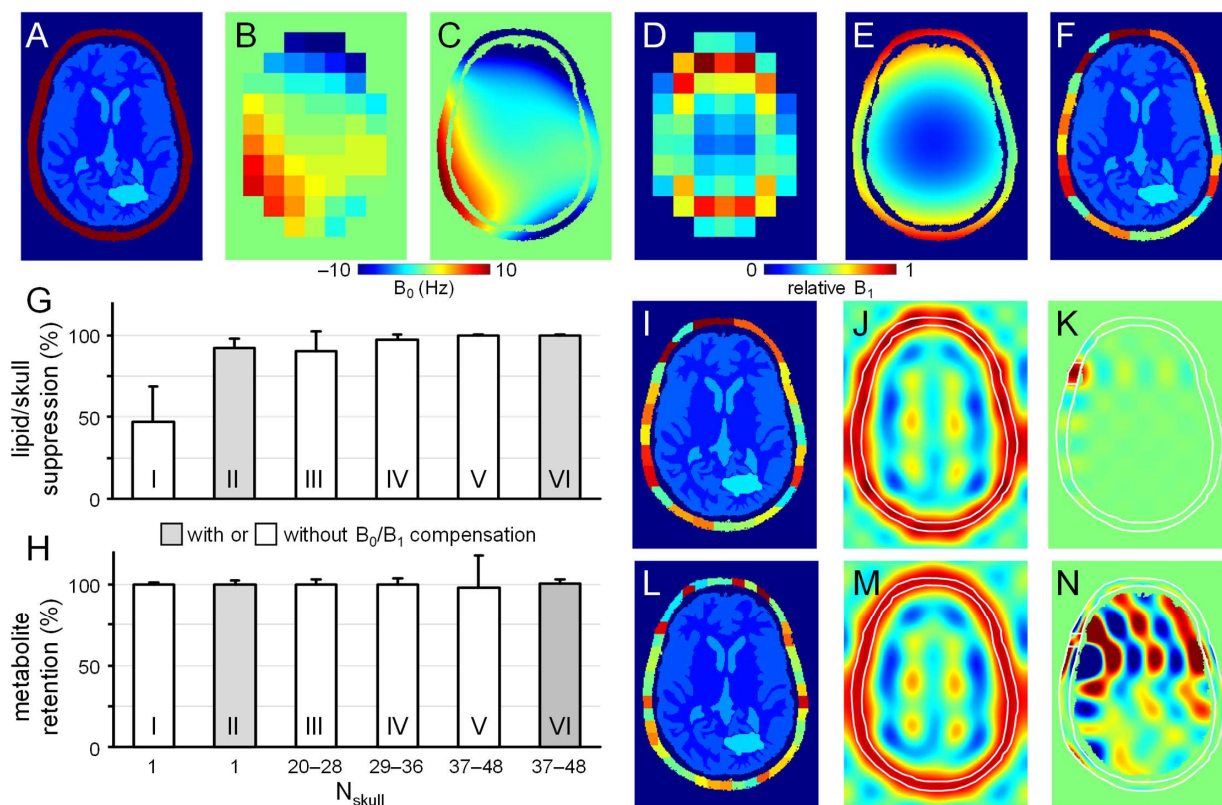
30

### 31 **3. RESULTS**

32 Fig. 2A shows the brain and non-brain ROIs used for one of the simulations, together with DMI-derived  $B_0$  (Fig.  
33 2B) and  $B_1$  (Fig. 2D) maps, as well as surrogate  $B_0$  (Fig. 2C) and  $B_1$  (Fig. 2E) obtained by fitting the low-resolution  
34 maps in Figs. 2B/D with third order 2D polynomials. The  $B_0$  magnetic field varied between  $-10$  and  $+10$  Hz over



- 1 the areas analyzed, whereby the relative  $B_1$  amplitude varied from 0.15 in the center of the brain to 1.00 near
- 2 the periphery.



- 3
- 4 Fig. 2F shows the subdivision of the non-brain ROI into 23 smaller ROIs, whereby separate simulations
- 5 investigated the effect of the number of non-brain ROIs. Supplemental Figure S1 show five additional datasets
- 6 used for simulation (out of a total of 50 datasets). All simulations achieved 100% skull-based signal removal and
- 7 100% brain signal retention in the absence of  $B_0$  and/or  $B_1$  heterogeneity. Even in the presence of  $B_0$  and  $B_1$



1 heterogeneity, perfect results were obtained provided that the *exact*  $B_0$  and  $B_1$  spatial distributions were  
2 incorporated according to Eq. [5]. However, in the presence of  $B_0$  and/or  $B_1$  heterogeneity, skull-based signal  
3 suppression was only  $47 \pm 21$  % when the skull ROI was not subdivided further (Fig. 2G, column I). When the  
4 reconstruction was supplemented with DMI-derived surrogate  $B_0$  and  $B_1$  maps, the skull-based signal  
5 suppression improved to  $92 \pm 6$  % (Fig. 2G, column II). It was observed that the combined effect of incorporating  
6 surrogate  $B_0$  and  $B_1$  maps (6.6 x reduction in residual lipids) was larger than that of the separate  $B_0$  (2.9 x  
7 reduction) or  $B_1$  (1.1 x reduction) maps.  $B_0$  compensation becomes less important, and the overall lipid  
8 suppression improves, as the spectroscopic linewidths becomes broader. Fig. 2G/H (columns III to VI) explores  
9 the effect of subdividing the skull into  $N_{\text{skull}}$  ROIs, with  $N_{\text{skull}}$  ranging from 20-28 (column III), 29-36 (column IV)  
10 and 37-48 (columns V and VI). Without compensation for  $B_0/B_1$  heterogeneity, the skull suppression increases  
11 with increasing  $N_{\text{skull}}$  as the smaller ROIs exhibit less heterogeneity across their volume (lipid suppression equals  
12  $90 \pm 12$ ,  $97 \pm 3$  and  $99 \pm 1$  % for column III - V). However, for higher  $N_{\text{skull}}$  the variability in metabolite retention  
13 increases from 3% (column III) to 4% (column IV) to 20% (column V). Supplemental Figure S2 summarizes  
14 metabolite brain retentions across separate brain ROIs (GM, WM, CSF, and pathology) and essentially mirror  
15 the trends seen across the entire brain (Fig. 2H). This effect can be understood by considering the SRF (Eq. [4])  
16 as demonstrated for  $N_{\text{skull}} = 23$  (Fig. 2I-K) and  $N_{\text{skull}} = 44$  (Fig. 2L-N). In the case of  $N_{\text{skull}} = 23$ , both the overall  
17 skull SRF (Fig. 2J), being the phase-sensitive sum of all  $N_{\text{skull}}$  ROIs, and an exemplary single skull ROI (Fig. 2K)  
18 are well-behaved with the bulk SRF intensity within the intended skull ROI locations. Small contributions inside  
19 the brain have a zero net integral due to phase cancellation. In the case of  $N_{\text{skull}} = 44$ , the overall skull SRF (Fig.  
20 2M) looks like that for  $N_{\text{skull}} = 23$  (Fig. 2J). However, the single skull ROI (Fig. 2N) has the bulk SRF intensity  
21 inside the brain. Even though the integrated SRF intensity across the brain is zero, the strong reliance on phase-  
22 sensitive signal cancellation can lead to alteration of the brain metabolite signal distribution in the presence of  
23 compartmental heterogeneity, such as simulated in Fig. 2H (column V). Supplemental Figure S3 summarizes  
24 the absolute-valued SRF brain contribution for every skull ROI when  $N_{\text{skull}}$  varies from 1 to 50. The SRF  
25 contribution across the brain ROI for any skull ROI is small and well-behaved for  $N_{\text{skull}}$  less than circa 35.  
26 However, when  $N_{\text{skull}} > 35$ , the SRF contribution sharply rises, resulting in localization that is highly dependent  
27 on phase cancellation – a condition that is violated in the presence of heterogeneity. When the  $B_0/B_1$   
28 heterogeneity is compensated with surrogate  $B_0/B_1$  maps (Fig. 2H, column VI), the metabolite retention variability  
29 is greatly reduced (from 20% (column V) to 3% (column VI)) as the large SRF intensity within the brain is properly  
30 phase-canceled. Overall, the simulation results in Fig. 2 indicate that the effects of  $B_0/B_1$  heterogeneity can be  
31 reduced through (1) compensation with surrogate  $B_0/B_1$  maps, (2) subdivision of the skull region into smaller  
32 ROIs, or both, and that the skull ROI subdivision needs to balance improvement in skull suppression with  
33 increased variability in metabolite retention. Since the optimal ROI subdivision in Fig. S3 is fairly broad, all 3D  
34 human DMI data was divided according to a grid of nominal DMI voxels without further optimization.

35 Fig. 3 shows the performance of SLIM-based skull removal on a patient with a glioblastoma tumor. Fig. 3A shows  
36 a  $T_2$ -weighted spin-echo MRI with the approximate tumor location outlined in red. The white dotted lines indicate

- 1 the in-plane DMI grid (8 mL nominal resolution). Fig. 3B shows a grid of  $^2\text{H}$  MR spectra extracted from the 3D
- 2 DMI dataset at the location of the green 2 x 2 grid (Fig. 3A).

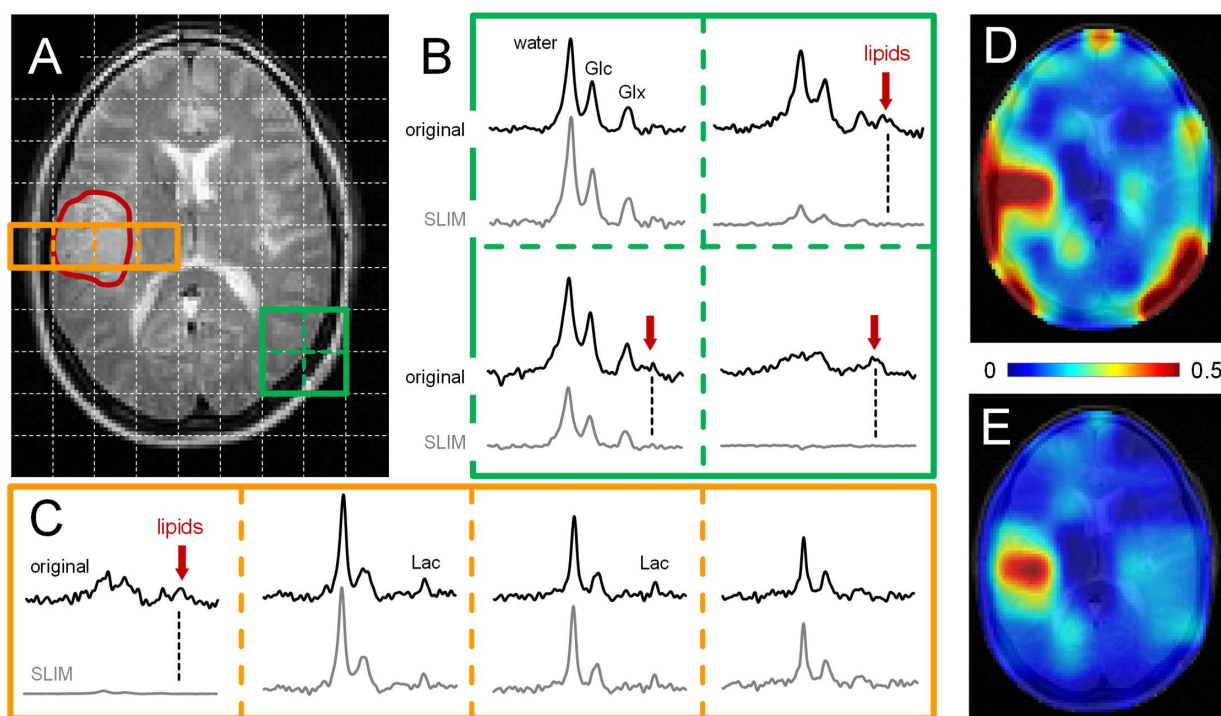


**Figure 3 – Performance of SLIM-based lipid signal removal on human brain *in vivo*.** (A) T<sub>2</sub>-weighted spin-echo MRI of a patient harboring a glioblastoma brain tumor with the approximate location outlined in red. The white dotted lines indicate the in-plane DMI grid (8 mL nominal resolution, circa 30 min total scan time). (B) 2 x 2 x 1 sub-grid extracted from the 9 x 13 x 11 DMI dataset showing the original (black, top) and SLIM-processed (gray, bottom)  $^2\text{H}$  MR spectra. In three spectra a clear natural abundance lipid signal (red arrow) is present in the original data which is completely removed following SLIM processing. (C) 4 x 1 x 1 sub-grid covering tumor and adjacent skull and brain tissue extracted from the 9 x 13 x 11 DMI dataset. Only the skull voxel shows a pronounced lipid signal that is removed with SLIM processing. While the remaining three spectra looks visually identical with or without SLIM processing, the removal of the extracranial lipid signal has a significant effect on the (D, E) resulting Lac/(Lac + Glx) metabolic maps.

- 3
- 4 The top spectra (black) represent the original, measured  $^2\text{H}$  MR spectra, whereas the bottom spectra (gray) are
- 5 obtained following SLIM-based skull suppression. Signals from the pure skull voxel (lower right) are completely
- 6 removed, whereas signals from the pure brain voxel (upper left) are fully retained. The two remaining voxel
- 7 locations have both brain and skull contributions. The extracranial signals (primarily lipids, both also glucose and
- 8 water) are suppressed, whereas the intracranial signals (glucose, glutamate, and water) are retained. Fig. 3C
- 9 shows a grid of  $^2\text{H}$  MR spectra extracted from the 3D DMI dataset at the location of the red 4 x 1 grid (Fig. 3A)
- 10 through the tumor region. Only the skull voxel shows a pronounced lipid signal that is removed with SLIM
- 11 processing. The remaining three spectra look visually identical with or without SLIM processing, with the



1 increased lactate signal within the tumor region remaining visibly unperturbed. However, the removal of  
2 extracranial lipid signal has a significant effect on the resulting Lac/(Lac + Glx) metabolic maps (Fig. 3D/E).  
3 Without skull suppression, the lipid signals lead to several hotspots surrounding the brain (Fig. 3D), including an  
4 artifactual elevation of the lactate signals within the tumor. After SLIM-based skull removal, the lipid hotspots are  
5 removed, resulting in a high-contrast ‘Warburg effect’ image of aberrant tumor metabolism (Fig. 3E). The lipid  
6 suppression across all subjects was  $90.5 \pm 11.4\%$  with 66% and 99% of all skull pixels achieving suppression  
7 factors of at least tenfold and threefold, respectively. The signal retentions for Glc and Glx were  $99.8 \pm 7.5$  and  
8  $100.2 \pm 7.8\%$ , respectively.

9

#### 10 **4. DISCUSSION**

11 The use of spatial prior knowledge in DMI processing allowed the removal of extracranial lipid signals in datasets  
12 acquired of human head to below the spectral noise level. Similar approaches have previously been used for  
13 lipid signal removal in  $^1\text{H}$  MRSI (Dong and Hwang, 2006; Adany et al., 2016). However,  $^1\text{H}$  MRSI requires lipid  
14 signal suppression factors well in excess of 100. This puts much higher demands on accurate prior knowledge  
15 and signal homogeneity and may ultimately place a limit on the robustness for use on  $^1\text{H}$  MRSI data. In contrast,  
16 the low natural abundance of deuterium leads to much lower amplitude lipid signals in the DMI data which were  
17 adequately removed with suppression factors below 10, thereby eliminating ambiguities in detecting elevated  
18 lactate levels.

19 The basic SLIM algorithm that uses two ROIs (one brain, one skull) without compensation for  $B_0$  and  $B_1$  magnetic  
20 field heterogeneity only provides modest lipid suppression ( $47 \pm 21\%$  in simulations). Subdividing the skull ROI  
21 into smaller compartments quickly improves the lipid suppression to  $>90$ ,  $>97$  and  $>99.5\%$  for  $\sim 25$ ,  $\sim 35$  and  
22  $\sim 45$  ROIs, respectively. However, improved lipid suppression is accompanied by more variable metabolite  
23 retention as the SRF outside any given ROI becomes more dominant and localization increasingly relies on  
24 phase cancellation. The inclusion of  $B_0$  and  $B_1$  maps greatly improved the lipid suppression (to  $92 \pm 6\%$  in  
25 simulations for one brain and one skull ROI) without increased variability in metabolite retention. The use of  
26 surrogate  $B_0$  and  $B_1$  maps based on the  $^2\text{H}$  water shift and intensity provide a practical solution to absence of  
27 high-resolution maps. Based on these results, it is recommended that  $B_0$  and  $B_1$  compensation should be used  
28 whenever possible, ideally in combination with a moderate subdivision of the skull ROI. It should be noted that  
29 while  $B_1$  heterogeneity was treated as a nuisance in the current implementation, it is possible to use  $B_1$  receive  
30 profiles for signal encoding to accelerate and/or improve data acquisition (An et al., 2011). While the average  
31 metabolite retention in the human brain *in vivo* is essentially 100%, the standard deviations on Glc and Glx are  
32 somewhat higher than anticipated compared to simulation results (Fig. 2). Several factors can explain the  
33 increased variability. Firstly, removal of extracranial signals, including water and Glc, will perturb brain signals  
34 as voxel bleeding due to the MRSI point spread function is also removed. Secondly, MRSI voxels with significant  
35 partial volume effects will be perturbed as extracranial contributions are selectively removed. Thirdly,



1 compensation of  $B_0$  and/or  $B_1$  heterogeneity with DMI-based surrogate  $B_0$  and/ $B_1$  maps will greatly decrease the  
2 variability in metabolite retention. However, since the surrogate maps are only an approximation of the actual  $B_0$   
3 and  $B_1$  heterogeneity, the compensation is necessarily incomplete, thus leading to some residual variability.  
4 Finally, the SNR of *in vivo* DMI data is generally low, such that small perturbations in signal shape or noise level  
5 can lead to large relative changes in fitted signal amplitude.

6 The SLIM implementation as presented here for DMI can be modified and extended in several ways to enhance  
7 the immunity to signal heterogeneity and improve the reliability. Sub-division of the skull ROI can be optimized  
8 further. The number of ROIs and ROI shapes can be based on (1) optimizing the SRF contributions, or (2) DMI-  
9 based lipid maps or (3) high-resolution MRI-based lipid maps. The SLIM algorithm is also ideally suited to allow  
10 regional analysis of brain ROIs during which  $^2\text{H}$  MR spectra can be obtained from anatomy-matched ROIs  
11 without partial volume effects. Development of automated definition of anatomical (GM, WM) and pathological  
12 (tumor core, tumor rim, FLAIR-enhanced) ROIs is currently in progress.

13 Similar levels of lipid suppression could have been achieved with alternative methods, such as dual density  
14 reconstruction (Hu et al., 1994; Metzger et al., 1999), data extrapolation (Haupt et al., 1996) or L2 regularization  
15 (Bilgic et al., 2014). Whereas L2 regularization and data extrapolation can operate on standard MRSI data, dual  
16 density reconstruction requires a modification of the data acquisition scheme, such that high k-space coordinates  
17 are sampled in addition to the standard low k-space coordinates typically acquired for MRSI. L2 regularization is  
18 based on the conditions of spatial and spectral orthogonality in which the desired and nuisance signals originate  
19 from spatially distinct compartments without spectral overlap. As the spectral overlap requirement cannot be  
20 fulfilled for lipids and lactate, L2 regularization will remove brain lactate signals, thus making it unsuitable for  
21 DMI. Like SLIM, data extrapolation only requires spatial separability of signals and would thus also be applicable  
22 to DMI. However, in the current investigation we focused on SLIM-based processing as the algorithm is readily  
23 extended to obtain signal from anatomy and/or pathology-based ROIs.

24

## 25 **CODE AVAILABILITY**

26 The Matlab code to process 3D DMI data, referred to as DMIWizard, is freely available for download from the  
27 Yale website or via GitHub (<https://github.com/radegraaf/DMIWizard>).

## 28 **COMPETING INTERESTS**

29 At least one of the (co-)authors is a member of the editorial board of Magnetic Resonance.

## 30 **ACKNOWLEDGEMENTS**

31 This research was funded, in part, by NIH grants NIBIB R01-EB025840 and R01- EB033764 and by CTSA grant  
32 KL2 TR001862 from the National Center for Advancing Translational Science (NCATS), component of the NIH  
33 and NIH roadmap for Medical Research.



## 1 REFERENCES

- 2 Adamson, P. M., Datta, K., Watkins, R., Recht, L., Hurd, R., and Spielman, D.: Deuterium Metabolic Imaging  
3 (DMI) for 3D mapping of glucose metabolism in humans with central nervous system lesions at 3T, *Magn  
4 Reson Med*, 2023.
- 5 Adany, P., Choi, I. Y., and Lee, P.: B<sub>0</sub>-adjusted and sensitivity-encoded spectral localization by imaging (BASE-  
6 SLIM) in the human brain *in vivo*, *Neuroimage*, 134, 355-364, 10.1016/j.neuroimage.2016.04.016, 2016.
- 7 Adany, P., Choi, I. Y., and Lee, P.: Method for fast lipid reconstruction and removal processing in (1) H MRSI of  
8 the brain, *Magn Reson Med*, 86, 2930-2944, 10.1002/mrm.28949, 2021.
- 9 An, L., Warach, S., and Shen, J.: Spectral localization by imaging using multielement receiver coils, *Magn  
10 Reson Med*, 66, 1-10, 10.1002/mrm.22783, 2011.
- 11 Bashir, A. and Yablonskiy, D. A.: Natural linewidth chemical shift imaging (NL-CSI), *Magn Reson Med*, 56, 7-18,  
12 10.1002/mrm.20917, 2006.
- 13 Bilgic, B., Chatnuntawech, I., Fan, A. P., Setsompop, K., Cauley, S. F., Wald, L. L., and Adalsteinsson, E.: Fast  
14 image reconstruction with L2-regularization, *J Magn Reson Imaging*, 40, 181-191, 10.1002/jmri.24365, 2014.
- 15 De Feyter, H. M., Behar, K. L., Corbin, Z. A., Fulbright, R. K., Brown, P. B., McIntyre, S., Nixon, T. W.,  
16 Rothman, D. L., and de Graaf, R. A.: Deuterium metabolic imaging (DMI) for MRI-based 3D mapping of  
17 metabolism *in vivo*, *Sci Adv*, 4, eaat7314, 10.1126/sciadv.aat7314, 2018.
- 18 Dong, Z. and Hwang, J. H.: Lipid signal extraction by SLIM: application to <sup>1</sup>H MR spectroscopic imaging of  
19 human calf muscles, *Magn Reson Med*, 55, 1447-1453, 2006.
- 20 Haupt, C. I., Schuff, N., Weiner, M. W., and Maudsley, A. A.: Removal of lipid artifacts in <sup>1</sup>H spectroscopic  
21 imaging by data extrapolation, *Magn Reson Med*, 35, 678-687, 1996.
- 22 Hesse, F., Somai, V., Kreis, F., Bulat, F., Wright, A. J., and Brindle, K. M.: Monitoring tumor cell death in murine  
23 tumor models using deuterium magnetic resonance spectroscopy and spectroscopic imaging, *Proc Natl Acad  
24 Sci U S A*, 118, e2014631118, 10.1073/pnas.2014631118, 2021.
- 25 Hu, X., Patel, M., and Ugurbil, K.: A new strategy for spectroscopic imaging, *J Magn Reson B*, 103, 30-38,  
26 1994.
- 27 Hu, X., Levin, D. N., Lauterbur, P. C., and Spraggins, T.: SLIM: spectral localization by imaging, *Magn Reson  
28 Med*, 8, 314-322, 1988.
- 29 Ip, K. L., Thomas, M. A., Behar, K. L., de Graaf, R. A., and De Feyter, H. M.: Mapping of exogenous choline  
30 uptake and metabolism in rat glioblastoma using deuterium metabolic imaging (DMI), *Front Cell Neurosci*,  
31 17, 1130816, 10.3389/fncel.2023.1130816, 2023.
- 32 Kaggie, J. D., Khan, A. S., Matys, T., Schulte, R. F., Locke, M. J., Grimmer, A., Frary, A., Menih, I. H., Latimer,  
33 E., Graves, M. J., McLean, M. A., and Gallagher, F. A.: Deuterium metabolic imaging and hyperpolarized  
34 <sup>13</sup>C-MRI of the normal human brain at clinical field strength reveals differential cerebral metabolism,  
35 *Neuroimage*, 257, 119284, 10.1016/j.neuroimage.2022.119284, 2022.



- 1 Khalidov, I., Van De Ville, D., Jacob, M., Lazeyras, F., and Unser, M.: BSLIM: spectral localization by imaging  
2 with explicit  $B_0$  field inhomogeneity compensation, *IEEE transactions on medical imaging*, 26, 990-1000,  
3 10.1109/tmi.2007.897385, 2007.
- 4 Kreis, F., Wright, A. J., Hesse, F., Fala, M., Hu, D. E., and Brindle, K. M.: Measuring tumor glycolytic flux *in vivo*  
5 by using fast deuterium MRI, *Radiology*, 294, 289-296, 10.1148/radiol.2019191242, 2020.
- 6 Liang, Z. and Lauterbur, P. C.: A theoretical analysis of the SLIM technique, *J Magn Reson B*, 102, 54-60,  
7 1993.
- 8 Liang, Z. P. and Lauterbur, P. C.: A generalized series approach to MR spectroscopic imaging, *IEEE*  
9 *transactions on medical imaging*, 10, 132-137, 10.1109/42.79470, 1991.
- 10 Liu, Y., De Feyter, H. M., Fulbright, R. K., McIntyre, S., Nixon, T. W., and de Graaf, R. A.: Interleaved Fluid-  
11 attenuated Inversion Recovery (FLAIR) MRI and Deuterium Metabolic Imaging (DMI) on human brain *in vivo*  
12 *Magn Reson Med*, 88, 28-37, 2022.
- 13 Markovic, S., Roussel, T., Neeman, M., and Frydman, L.: Deuterium Magnetic Resonance Imaging and the  
14 Discrimination of Fetoplacental Metabolism in Normal and L-NAME-Induced Preeclamptic Mice, *Metabolites*,  
15 11, 376, 10.3390/metabo11060376, 2021.
- 16 Metzger, G., Sarkar, S., Zhang, X., Heberlein, K., Patel, M., and Hu, X.: A hybrid technique for spectroscopic  
17 imaging with reduced truncation artifact, *Magn Reson Imaging*, 17, 435-443, 10.1016/s0730-725x(98)00187-  
18 8, 1999.
- 19 Passeri, A., Mazzuca, S., and Bene, V. D.: Radiofrequency field inhomogeneity compensation in high spatial  
20 resolution magnetic resonance spectroscopic imaging, *Phys Med Biol*, 59, 2913-2934, 10.1088/0031-  
21 9155/59/12/2913, 2014.
- 22 Riis-Vestergaard, M. J., Laustsen, C., Mariager, C., Schulte, R. F., Pedersen, S. B., and Richelsen, B.: Glucose  
23 metabolism in brown adipose tissue determined by deuterium metabolic imaging in rats, *Int J Obes (Lond)*,  
24 44, 1417-1427, 10.1038/s41366-020-0533-7, 2020.
- 25 Ruhm, L., Avdievich, N., Ziegs, T., Nagel, A. M., De Feyter, H. M., de Graaf, R. A., and Henning, A.: Deuterium  
26 metabolic imaging in the human brain at 9.4 Tesla with high spatial and temporal resolution, *Neuroimage*,  
27 244, 118639, 10.1016/j.neuroimage.2021.118639, 2021.
- 28 Seres Roig, E., De Feyter, H. M., Nixon, T. W., Ruhm, L., Nikulin, A. V., Scheffler, K., Avdievich, N. I., Henning,  
29 A., and de Graaf, R. A.: Deuterium metabolic imaging of the human brain *in vivo* at 7 T, *Magn Reson Med*,  
30 89, 29-39, 10.1002/mrm.29439, 2022.
- 31 Straathof, M., Meerwaldt, A. E., De Feyter, H. M., de Graaf, R. A., and Dijkhuizen, R. M.: Deuterium metabolic  
32 imaging of the healthy and diseased brain, *Neuroscience*, 474, 94-99, 10.1016/j.neuroscience.2021.01.023,  
33 2021.
- 34 Tkáč, I., Deelchand, D., Dreher, W., Hetherington, H., Kreis, R., Kumaragamage, C., Považan, M., Spielman, D.  
35 M., Strasser, B., and de Graaf, R. A.: Water and lipid suppression techniques for advanced  $^1\text{H}$  MRS and



- 1 MRSI of the human brain: Experts' consensus recommendations, *NMR Biomed*, 34, e4459,  
2 10.1002/nbm.4459, 2021.
- 3 Veltien, A., van Asten, J., Ravichandran, N., de Graaf, R. A., De Feyter, H. M., Oosterwijk, E., and Heerschap,  
4 A.: Simultaneous Recording of the Uptake and Conversion of Glucose and Choline in Tumors by Deuterium  
5 Metabolic Imaging, *Cancers (Basel)*, 13, 10.3390/cancers13164034, 2021.
- 6 von Kienlin, M. and Mejia, R.: Spectral localization with optimal pointspread function, *J Magn Reson*, 94, 268-  
7 287, 1991.
- 8 Wang, T., Zhu, X. H., Li, H., Zhang, Y., Zhu, W., Wiesner, H. M., and Chen, W.: Noninvasive assessment of  
9 myocardial energy metabolism and dynamics using in vivo deuterium MRS imaging, *Magn Reson Med*, 86,  
10 2899-2909, 10.1002/mrm.28914, 2021.
- 11 Zhang, Y., Gabr, R. E., Schar, M., Weiss, R. G., and Bottomley, P. A.: Magnetic resonance Spectroscopy with  
12 Linear Algebraic Modeling (SLAM) for higher speed and sensitivity, *J Magn Reson*, 218, 66-76,  
13 10.1016/j.jmr.2012.03.008, 2012.

14

## 15 **FIGURE LEGENDS**

16 **Figure 1 – Lipid removal workflow.** (A) Anatomical MRI and (B) brain and non-brain/skull ROIs. (C) To  
17 accommodate heterogeneity in the skull ROI, it is sub-divided into 125-175 ROIs of 3.5 – 8.5 mL. (D)  $^2\text{H}$ -water  
18 map obtained through numerical integration of each pixel in a  $9 \times 13 \times 11$  DMI dataset. (E)  $^2\text{H}$ -water line shift  
19 map and (F) relative  $^2\text{H}$ -water intensity map. (G) Compartment-specific signals from one brain ROI and 143 skull  
20 ROIs are the primary output of the SLIM algorithm. (H) DMI reconstructed from the 143 skull ROI signals, which  
21 can be subtracted from (D) the original DMI to yield (I) a skull (and lipid) free DMI dataset.

22

23 **Figure 2 – Performance of SLIM-based lipid signal removal on phantoms *in silico*.** (A) Brain and skull tissue  
24 constellation for one out of 50 permutations. (B) Water shift and (D) intensity maps as extracted from DMI data,  
25 providing (C) surrogate  $B_0$  and (E)  $B_1$  maps following low-order polynomial fitting. (F) ROI map with the skull ROI  
26 subdivided into 23 smaller compartments (i.e.,  $N_{\text{skull}} = 23$ ) to accommodate signal heterogeneity. (G) Lipid  
27 suppression and (H) metabolite retention under different scenarios including  $N_{\text{skull}} = 1$  without (column I) and with  
28 (column II)  $B_0$  and  $B_1$  compensation,  $N_{\text{skull}} = 20$ -28 (column III), 29-36 (column IV), 37-48 (columns V and VI)  
29 without (columns III-V) and with  $B_0$  and  $B_1$  compensation (column VI). Results for the separate brain ROIs (GM,  
30 WM, CSF and pathology) are summarized in Supplemental Figure S2 and essentially minor the whole brain  
31 results shown in (H). (I, L) Head constellations with the skull ROI subdivided into (I) 23 and (L) 44 smaller  
32 compartments. (J, K, M, N) Spatial response function (SRF) of (J, M) the summed skull ROIs and (K, N) a single  
33 skull ROI for  $N_{\text{skull}} = 23$  (J, K) and  $N_{\text{skull}} = 44$  (M, N). All SRFs have the same vertical scale, spanning -1 to +1.  
34 While the integrated, *phase-sensitive* SRF intensity of a single skull ROI is zero across the brain ROI for any



1  $N_{\text{skull}}$ , the integrated, *absolute-valued* SRF intensity will be much larger for  $N_{\text{skull}} = 44$  (N) compared to  $N_{\text{skull}} = 23$   
2 (K). Supplemental Figure S3 gives a summary of the absolute-valued SRF across the brain ROI for  $N_{\text{skull}}$  ranging  
3 from 1 to 50.

4  
5 **Figure 3 – Performance of SLIM-based lipid signal removal on human brain *in vivo*.** (A)  $T_2$ -weighted spin-  
6 echo MRI of a patient harboring a glioblastoma brain tumor with the approximate location outlined in red. The  
7 white dotted lines indicate the in-plane DMI grid (8 mL nominal resolution, circa 30 min total scan time). (B) 2 x  
8 2 x 1 sub-grid extracted from the 9 x 13 x 11 DMI dataset showing the original (black, top) and SLIM-processed  
9 (gray, bottom)  $^2\text{H}$  MR spectra. In three spectra a clear natural abundance lipid signal (red arrow) is present in  
10 the original data which is completely removed following SLIM processing. (C) 4 x 1 x 1 sub-grid covering tumor  
11 and adjacent skull and brain tissue extracted from the 9 x 13 x 11 DMI dataset. Only the skull voxel shows a  
12 pronounced lipid signal that is removed with SLIM processing. While the remaining three spectra looks visually  
13 identical with or without SLIM processing, the removal of the extracranial lipid signal has a significant effect on  
14 the (D, E) resulting Lac/(Lac + Glx) metabolic maps.